IOPscience iopscience.iop.org

Home Search Collections Journals About Contact us My IOPscience

Ion production cost of a gridded helicon ion thruster

This content has been downloaded from IOPscience. Please scroll down to see the full text.

2013 Plasma Sources Sci. Technol. 22 055019

(http://iopscience.iop.org/0963-0252/22/5/055019)

View the table of contents for this issue, or go to the journal homepage for more

Download details:

IP Address: 128.61.62.132
This content was downloaded on 02/10/2013 at 19:24

Please note that terms and conditions apply.

Plasma Sources Sci. Technol. **22** (2013) 055019 (10pp) doi:10.1088/0963-0252/22/5/055019

Ion production cost of a gridded helicon ion thruster

Logan T Williams and Mitchell L R Walker

Department of Aerospace Engineering, Georgia Institute of Technology, 270 Ferst Drive, Atlanta, GA, USA

Received 23 April 2013, in final form 2 August 2013
Published 27 September 2013
Online at stacks.iop.org/PSST/22/055019

Abstract
Helicon plasma sources are capable of efficiently ionizing propellants and have been considered for application in electric propulsion. However, studies that estimate the ion production cost of the helicon plasma source are limited and rely on estimates of the extracted ion current. The ion production cost of a helicon plasma source is determined using a gridded ion thruster configuration that allows accurate measurement of the ion beam current. These measurements are used in conjunction with previous characterization of the helicon plasma to create a model of the discharge plasma within the gridded thruster. The device is tested across a range of operating conditions: 343–600 W radio frequency power at 13.56 MHz, 50–250 G and 1.5 mg s^{-1} of argon at a pressure of 1.6×10^{-5} Torr-Ar. The ion production cost is 132–212 ± 28–46 eV/ion, driven primarily by ion loss to the walls and anode, as well as energy loss in the anode and grid sheaths.

(Some figures may appear in colour only in the online journal)

1. Introduction

A helicon plasma source is a highly efficient device capable of creating a high-density, low-temperature plasma using radio frequency (rf) waves transmitted from an antenna [1–7]. Proposed applications of helicon sources have included plasma processing, ion laser pumping, toroidal plasmas and ion sources for electric propulsion. For the particular application as an ion source for electric propulsion devices, the aim is to replace direct current (dc) collisional discharges that are currently used in most devices. This requires the effective energy cost for the helicon source to create an extracted ion to be less than that of dc discharges. The ion production cost, sometimes referred to as the discharge loss, is higher than the ionization energy, as not only is power expended to first create the ion, but also in various loss mechanisms such as recombination, collisional excitation and wall neutralization. Thus, the discharge efficiency is a measure of the energy cost to create and transport an ion to the grids taking these losses into account. Generally, the discharge efficiency is about a factor of ten greater than the ionization cost [8].

While helicon plasma sources have been observed to create high-density plasmas, there is limited experimental measurement of the actual ion production cost. There are two components to determining the ion production cost: measurement of the extracted ion current and estimation of the power expenditure in the discharge plasma. Previous research has relied on measurements of the ion current using multiple planar Langmuir probes downstream [9], or through measurements of the helicon plasma density using a Langmuir probe and assuming some overall ion diffusion [10]. The difficulty with the first approach is that probes within a plasma form a plasma sheath, which tends to increase the collection area and overestimate the overall ion current. The second approach neglects the plasma structure, which strongly impacts ion diffusion rates, and assumes an ion exit velocity without direct measurements. The use of either method results in an inaccurate measurement of the extracted ion current.

One reason for the difficulty in measuring the extracted current is the fact that the helicon source is an electrodeless ionization source that exhausts a quasi-neutral plasma. If the helicon source instead exhausted solely ions, an electrode inside the plasma discharge would be required to collect an equivalent electron current to maintain charge balance, i.e. an anode. This is often the case when a helicon plasma source is integrated into an accelerated ion extraction system, such as an ion thruster. However, such configurations introduce other considerations to measuring the ion current.

 © 2013 IOP Publishing Ltd Printed in the UK & the USA

A study on a two-stage helicon thruster also had difficulty in determining the ion production cost, as the Hall thruster stage allows electron backstreaming to the anode, which prevents accurate measurements of the beam current [11]. A gridded ion extractor eliminates electron backstreaming, as the downstream grid can be biased below the downstream plasma potential to repel electrons. This results in an anode current that is equal to the extracted ion current at the grids, which can be easily measured.

The second component to determining the ion production cost is the power expended to generate the extracted ion current. In previous studies, this power was approximated as the transmitted power to the antenna. However, some of the RF power can be coupled to the solenoid mounts, or capacitively coupled to ground through the vacuum chamber. Furthermore, such an approach does not allow for a closer examination of the possible loss mechanisms that affect the ion production cost. A more detailed approach is to measure the discharge plasma structure and construct a model of the ion currents and sheath potentials present within the discharge chamber. This enables comparisons of each ion loss source and estimation of power deposition into the plasma, as well as the key operating parameters that impact these losses.

Therefore, the method used to determine the ion production cost of the helicon plasma source is to combine the helicon source with electrostatic grids and an anode as used in ion engines. This allows an accurate means to measure the extracted ion current, as the current through the grids and anode can be measured, while the grids prevent electron backstreaming into the discharge chamber. Additionally, the grids can be removed to measure the shape of the plasma structure, specifically the plasma potential, ion number density and electron temperature. These values can be used to construct a model of the helicon discharge plasma and estimate the absorbed RF power and ion loss mechanisms. The device is tested across a range of operating conditions: 343–600 W RF power at 13.56 MHz, 50–250 G and 1.5 mg s^{-1} of argon at a pressure of 1.6×10^{-5} Torr-Ar.

2. Experimental setup

Determination of the ion production cost requires two stages: measurement of the discharge plasma structure of the helicon plasma source, and measurement of the extracted ion current in the gridded configuration. In order for the combination of the two data sets to be valid, both configurations must use identical helicon source geometry. Therefore, the simplest method is to use the same helicon source and add the components required to complete the gridded ion engine. Full characterization of the helicon plasma source [12] and of the gridded engine [13] is discussed elsewhere [14], but descriptions of the devices and a sample of the data are included for clarity.

2.1. Helicon plasma source

The helicon consists of a Pyrex discharge chamber 27.3 cm long and 14.0 cm in diameter. The axial magnetic field is provided by two 725-turn solenoids 7.6 cm wide with an inner diameter of 19.7 cm. The solenoids are placed 10.2 cm apart. The matched-line loss is 0.65 dB, which includes attenuation caused by the feedthrough. During testing the SWR ranged from 1.01 to 1.04, which results at most in an additional 0.0004 dB of attenuation. A full description of the helicon plasma source is available elsewhere [14, 15].

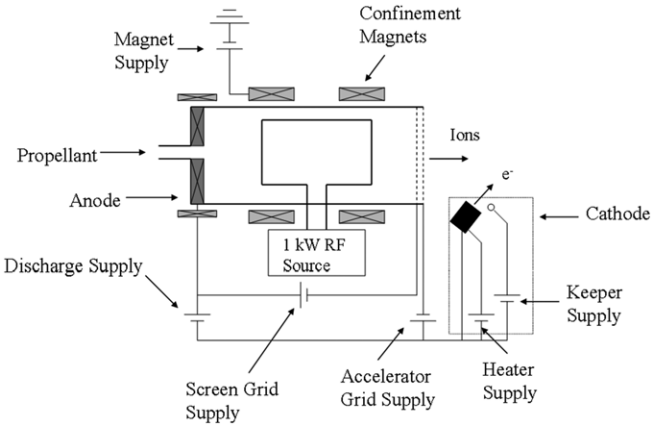

Figure 1. GHIT configuration.

2.2. Gridded helicon ion thruster

There are three subsystems to the gridded helicon ion thruster (GHIT): the helicon plasma source, the electrostatic grid assembly and the thruster discharge circuit. The helicon discharge serves to ionize the propellant; the grid assembly extracts the ions from the discharge chamber, and the anode–cathode circuit biases the discharge plasma to create a net potential drop to accelerate the ions and extracts electrons to neutralize the beam. Figure 1 shows the configuration of the thruster.

2.2.1. Grid assembly. The grid assembly consists of two stainless steel grids, the screen and accel, and an insulated support structure that maintains a set separation between the grids. The screen grid aperture diameter is 1.5 mm, with the accel grid aperture diameter 1.2 mm. The grid thickness is 0.635 mm and the grid separation distance is 1.0 mm. Both grids are laser-cut from SS 316 with the apertures arranged in a 60° hexagonal pattern with a pitch of 1.75 mm. During operation, the screen grid is biased 35 V below the anode, and the accel grid is biased 150 V below the cathode.

2.2.2. Thruster discharge circuit. The final subsystem is the thruster discharge circuit, which consists of an anode placed inside the discharge chamber and a cathode mounted downstream of the grid assembly. The thruster discharge circuit serves two functions. The first is to bias the plasma potential within the discharge chamber. The net energy of the ions leaving the thruster is determined not by the potential drop across the grids, but by the net potential drop between the discharge plasma and the space potential. The discharge voltage is the potential difference between the anode and the cathode supplied by the discharge power supply. The second

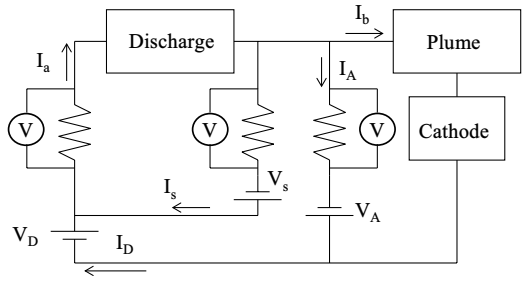

Figure 2. GHIT thruster circuit.

purpose of the thruster discharge circuit is to allow a connection between the neutralizer cathode and the discharge plasma. The anode is a 6.5 mm thick stainless steel 316 disk with an outer diameter of 13.85 cm placed at the inlet side of the interior of the discharge chamber. A 1.59 mm diameter, 25 mm long stainless steel rod is welded to the back of the anode and extends through a sealed hole in the back of the discharge chamber to allow for an electrical connection to the anode. The cathode is a lanthanum hexaboride (LaB_6) hollow cathode following the design of the Moscow Aviation Institute.

2.2.3. Discharge circuit measurement. The thruster circuit is a conceptualization of the schematic shown in figure 1. The discharge plasma is treated as a conductive element that connects the grids and the anode. The grids and the anode act as direct connections from the discharge plasma to the respective power supplies that provide the component potential. The anode is assumed to collect a net electron current, which results in a positive current into the discharge. The grids are assumed to collect only ions, and thus are depicted as positive currents out of the discharge. Any ion current that is not collected by either the screen or the accel grid is assumed to enter the plume as part of the ion beam. This ion current must be neutralized by an electron current of equal magnitude from the cathode, which is connected to the discharge supply. This electron current is represented as a positive current flowing to the discharge supply from the cathode. The individual currents collected by the anode and the grids are determined by measuring the voltage across three resistor shunts. The resistances of the shunts for the anode, screen grid and accel grid are 5.085 Ω, 5.095 Ω and 5.079 Ω, respectively. Figure 2 shows the thruster circuit. It should be noted that while the screen and accel grids are biased below the anode and cathode, respectively, they are reported by their magnitudes.

Using Kirchhoff's junction rule at the discharge, the beam current, I_b, can be defined from figure 2 as

$$I_b = I_a - I_s - I_A \tag{1}$$

where I_a is the anode current, I_s is the screen grid current and I_A is the accel grid current. The voltages across the resistor shunts are measured using three Fluke 83 V multimeters. The Fluke 83 V has an uncertainty of ±0.3% of the measured value for the measurement range used. The shunt resistance is measured with an Agilent U1733C RLC meter with an accuracy of ±0.7%+0.008 Ω for the 20 Ω range used. The total uncertainty of the current measurements is ±0.9%.

2.3. Facility and diagnostics

All experiments are conducted in the Vacuum Test Facility 1 (VTF-1) [14, 15]. The base pressure of VTF-1 for these experiments is 1.1×10^{-5} Torr with an effective pumping speed of 125 000 l s^{-1} for argon. Measurements are performed using a floating emissive probe and a Langmuir probe mounted on a two-axis linear motion system. The linear tables are 1.5 m long model of the 406XR series by Parker Automation with a positional accuracy of ±134 μm and a bidirectional repeatability of ±3.0 μm. Full details of the probes are found elsewhere, but summaries are given for clarity [14].

The basic premise of a floating emissive probe is to remove the plasma sheath between the probe and the bulk plasma, and allow a direct measurement of the plasma potential. The probe utilizes a heated tungsten filament to thermionically emit electrons to break down the sheath. The filament is heated by passing a current through the filament in a floating dc circuit. As the filament current is progressively increased, the electron emission increases and decreases the difference in potential between the filament and the plasma. At a sufficient current, the sheath is completely removed and the filament floats at the plasma potential. The average uncertainty of the probe is ±4.36 V.

A Langmuir probe is used in conjunction with the floating emissive probe to determine the electron temperature and density. Using the measurements of the plasma potential made with the emissive probe, the electron temperature can be calculated from measurements of the floating potential:

$$V_p - V_f = -\frac{k_b T_e}{e} \ln\left(0.61\sqrt{\frac{2\pi m_e}{m_i}}\right). \tag{2}$$

The uncertainty with this method is ±17% [16]. The electron number density can be calculated from the ion saturation current using equation (3) and the area of the probe, A_p:

$$I_{sat} = 0.61 e n_0 A_p \left(\frac{k_b T_e}{m_i}\right)^{1/2}. \tag{3}$$

3. Discharge model

The ion production cost is the ratio of the power absorbed by the plasma from the RF system, P_{abs}, to the beam current created:

$$\eta_d = \frac{P_{abs}}{I_b}. \tag{4}$$

The units of ion production cost are W A^{-1}, or more commonly eV per ion. Rather than model energy absorption from the antenna to the plasma, the amount of energy deposited into the plasma can be modeled by the power expended by the plasma. There are several pathways for energy to exit the discharge. The primary energy expenditures are neutral ionization, neutral excitation, ion current flow to the grids and discharge chamber wall, ion current to the beam, electron flow to the wall and electron collection by the anode. Since a Child–Langmuir sheath exists at the grids, the electron current to the grids is negligible. In the steady state, the power absorbed by the

plasma must equal the power output, which can be written as [8]

$$P_{\text{abs}} = \underbrace{I_{\text{p}}\varepsilon^{+} + I^{*}\varepsilon^{*}}_{\text{Ionization \& excitation}} + \underbrace{(I_{\text{s}} + I_{\text{b}} + I_{\text{A}})\left(\frac{k_{\text{b}}T_{\text{e}}}{2} + \phi_{\text{s}}\right)}_{\text{Grid ion extraction loss}} + \underbrace{I_{\text{w,i}}\left(\frac{k_{\text{b}}T_{\text{e}}}{2} + \phi_{\text{w}}\right)}_{\text{Wall ion loss}} + \underbrace{I_{\text{w,e}}(2k_{\text{b}}T_{\text{e}} + \phi_{\text{w}})}_{\text{Wall electron loss}} + \underbrace{I_{\text{a,i}}\left(\frac{k_{\text{b}}T_{\text{e}}}{2} + \phi_{\text{a}}\right)}_{\text{Anode ion loss}} + \underbrace{I_{\text{a,e}}(2k_{\text{b}}T_{\text{e}} + \phi_{\text{a}})}_{\text{Anode electron loss}} \quad (5)$$

where I^{*} is the rate of neutral excitation, I_{s} is the ion current to the screen grid, I_{b} is the ion beam current, I_{A} is the accel grid current, $I_{\text{w,i}}$ is the rate of ion loss to the walls, $I_{\text{w,e}}$ is the electron loss rate to the walls, $I_{\text{a,e}}$ is the electron current to the anode, $I_{\text{a,i}}$ is the ion current to the anode, ε is the energy of ionization and excitation and φ_j is the potential difference of the sheath between the discharge plasma potential and j, where j is s, w or a for the screen grid, the wall or the anode, respectively.

The ion production rate can be expressed as a function of the ionization cross section of the neutral particle, σ_{i}, the volume of the discharge chamber, V_{d}, and the electron velocity, v_{e}:

$$I_{\text{p}} = n_{\text{n}}n_{\text{e}}\langle\sigma_{\text{i}}v_{\text{e}}\rangle V_{\text{d}}. \quad (6)$$

The term in the brackets denotes the product averaged over the Maxwellian distribution of the electron velocity distribution function. The neutral excitation rate can similarly be expressed as

$$I^{*} = n_{\text{n}}n_{\text{e}}\langle\sigma^{*}v_{\text{e}}\rangle V_{\text{d}} \quad (7)$$

with the total excitation collision cross section for a 15 eV electron and a neutral argon atom being approximately $0.1 \times 10^{-20}\,\text{m}^2$ [17]. Neutral density is determined from a numerical model of the discharge chamber [18].

Ideally, the beam current is the Bohm current into the open area of the screen grid, which is the grid area, A_{g}, multiplied by the screen grid transparency, T_{s}:

$$I_{\text{b}} = 0.61 n_0 e A_{\text{g}} T_{\text{s}} v_{\text{Bohm}}. \quad (8)$$

The transparency is defined as the ratio of the open area of the grid to the total area occupied by the grid:

$$T_{\text{s}} = \frac{A_{\text{g,open}}}{A_{\text{g}}}. \quad (9)$$

This is a reasonable approximation for the sheath area, since the slightly convex shape of the sheath does not appreciably add to the surface area compared with the open area of the grids. However, equation (8) assumes there is no ion impingement on the accel grid, which is not always the case. Instead, it is more accurate to state that the Bohm current is equal to the combined accel grid and beam currents:

$$I_{\text{b}} + I_{\text{A}} = 0.61 n_0 e A_{\text{g}} T_{\text{s}} v_{\text{Bohm}}. \quad (10)$$

Similarly, the screen grid current is the Bohm current into the closed area of the screen grid:

$$I_{\text{s}} = 0.61 n_0 e A_{\text{g}}(1 - T_{\text{s}}) v_{\text{Bohm}}. \quad (11)$$

The possibility exists that the anode will still collect an ion current from the discharge plasma. This occurs when the area of the anode is comparable to the area of the grids, or when the anode does not draw a very large current. Assuming that the anode collects both ions and electrons, the currents to the anode are

$$I_{\text{a,e}} = \frac{1}{4} e n_0 A_{\text{a}} \left(\frac{8k_{\text{b}}T_{\text{e}}}{\pi m_{\text{e}}}\right)^{1/2} \exp\left(\frac{e\phi_{\text{a}}}{k_{\text{b}}T_{\text{e}}}\right) \quad (12)$$

$$I_{\text{a,i}} = 0.61 e n_0 A_{\text{a}} \left(\frac{k_{\text{b}}T_{\text{e}}}{m_{\text{i}}}\right)^{1/2} \quad (13)$$

where A_{a} is the area of the anode.

The ion and electron currents to the discharge chamber wall differ from the other currents into a sheath due to the presence of the axial magnetic field. The magnetic field does not limit the electron mobility parallel to the magnetic field, such as to the anode; however, it does limit the transverse electron mobility, such as the electron flow to the wall. Electrons are thus confined to the magnetic field lines and can only achieve transverse diffusion via collisions. The ion gyroradius is much larger than the electron gyroradius, and ions are much less confined than electrons. In order to maintain quasi-neutrality ions must exit the discharge chamber (in this case by neutralizing at the wall) at the same rate as electrons, which requires ion mobility to be decreased. As a result, an electric field arises that accelerates electrons and decelerates ions, a mechanism called ambipolar diffusion. The transverse velocity for an ion or electron for ambipolar diffusion is expressed as [8]

$$v_{\perp} = \frac{\mu_{\text{e}}}{1 + \mu_{\text{e}}^2 B^2 - (\nu_{\text{ei}}/\nu_{\text{e}})}\left(E_{\perp} + \frac{k_{\text{b}}T_{\text{e}}}{e}\frac{\nabla n_{\text{e}}}{n_{\text{e}}}\right) \quad (14)$$

where μ_{e} is the transverse electron mobility, B is the applied magnetic field strength and ν is the collision frequency, with the subscript 'ei' denoting electron–ion collisions and 'e' denoting electron collisions with either ions or neutrals. The above terms are defined as

$$\mu_{\text{e}} = \frac{e}{m_{\text{e}}\nu_{\text{e}}} \quad (15)$$

$$\nu_{\text{e}} = \nu_{\text{en}} + \nu_{\text{ei}} \quad (16)$$

$$\nu_{\text{ei}} = n_{\text{i}}\sigma_{\text{ei}}\bar{v}_{\text{e}} \quad (17)$$

while the electron–neutral collision frequency is [19]

$$\nu_{\text{en}} = 5 \times 10^{-19} n_{\text{n}} \sqrt{\frac{k_{\text{b}}T_{\text{e}}}{m_{\text{e}}}}. \quad (18)$$

The average electron collision velocity is a function of the reduced mass, m^{*}, so the following can be said:

$$\bar{v}_{\text{e}} = \sqrt{\frac{8k_{\text{b}}T_{\text{e}}}{\pi m_{\text{e,i}}^{*}}} \quad (19)$$

$$m^*_{e,i} = \frac{m_e m_i}{m_e + m_i} \approx m_e. \tag{20}$$

For Coulomb collisions, the cross section is

$$\sigma_{ei} = \frac{e^4 \ln \Lambda}{16\pi \varepsilon_0^2 k_b^2 T_e^2} \tag{21}$$

where $\ln \Lambda$ is the Coulomb logarithm, defined in terms of the Debye length, λ_D:

$$\Lambda = 12\pi n_e \lambda_D^3 \tag{22}$$

$$\lambda_D = \left(\frac{\varepsilon_0 k_b T_e}{e^2 n_0}\right)^{1/2}. \tag{23}$$

Substituting equations (19)–(22) into equation (17) yields

$$\nu_{ei} = n_i \frac{e^4}{\varepsilon_0^2 (32 m_e)^{1/2} (\pi k_b T_e)^{3/2}} \ln(12\pi n_e \lambda_D^3). \tag{24}$$

The ion and electron wall currents are thus

$$I_{w,i} = I_{w,e} = n_0 e A_w v_\perp. \tag{25}$$

The anode sheath potential is defined in relation to the discharge temperature by enforcing charge balance and equating the ion currents to the electron currents:

$$I_{a,e} + I_{w,e} = I_{a,i} + I_{w,i} + I_s + I_A + I_b. \tag{26}$$

Substituting equations (10), (11), (12), (13) and (25) into equation (26) yields

$$\phi_a = \frac{k_b T_e}{e} \ln\left(0.61 \frac{A_a + A_g}{A_a} \sqrt{\frac{2\pi m_e}{m_i}}\right). \tag{27}$$

Thus, unless the grid area is much larger than the anode area, equation (27) contains the natural log of a quantity less than one, which yields a negative anode sheath potential. This confirms the earlier assumption that the anode sheath collects ions in addition to electrons. Physically, this is due to the higher velocity of the electrons creating a larger electron current incident on the anode than is required to balance the grid currents. In order to maintain charge balance, the anode sheath must repel some of the electrons, which necessitates a negative sheath potential and the collection of ions.

The sheath potential to the screen grid can be found by relating the anode and screen potentials to the anode sheath potential:

$$\phi_s = \phi_a - (V_a - V_s). \tag{28}$$

If a cylindrical discharge chamber is assumed with an axial magnetic field, and the only insulating wall condition is on the radial boundary, then the ion and electron wall collision rates are already equal due to ambipolar diffusion across a magnetic field. Therefore, no wall potential is required to ensure quasi-neutrality and φ_w is zero.

4. Results

There are two components to the ion production cost: the extracted current and the power absorbed by the plasma. While the extracted current can be directly measured from operation of the GHIT, one of the key power loss terms is ion loss to the discharge chamber walls. In order to model this quantity, measurements of the shape of the discharge plasma are required.

4.1. Discharge plasma characterization

From equation (14), two quantities of interest for modeling ion loss to the walls are the radial electric field and the radial component of the ion number density gradient. Both values can be calculated using a difference quotient of the plasma potential and ion number density, respectively. Figures 3 and 4, respectively, show a sample set of contour plots of the plasma potential and ion number density at 150 G and 350 G.

4.2. Gridded ion extraction

Figure 5 shows a sample breakdown of the component currents. The anode current is relatively constant with respect to the discharge voltage, with only a 2.3% variation across the range of voltages tested. In contrast, the grid and beam currents are strongly dependent on the value of the discharge voltage, as it sets the total potential drop between the grids. This demonstrates that while the ion optics of the grids is sensitive to the discharge voltage, the total ion current extracted to the grid sheath is independent of the discharge voltage. Instead, the extracted current is a function of the rf power and the axial magnetic field strength, as these parameters impact the ion number density and electron temperature, which determine the Bohm current. Figure 6 shows the extracted current as a function of rf power and magnetic field strength.

The average ion number density and electron temperature can be estimated by using the screen grid as a planar Langmuir probe [13, 14]. Figures 7 and 8 show the average ion number density and electron temperature, respectively, as a function of rf power and magnetic field strength. Increasing the rf power is shown to increase both the ion density and the electron temperature, but a larger impact is achieved with the magnetic field strength. For the ion number density, the effect of the magnetic field is monotonic, but for the electron temperature this is not the case.

5. Discussion

The model is solved using data from both configurations at 343 and 600 W at 150 G and a discharge voltage of 600 V. The plasma is assumed to have averaged characteristics represented by a single value each for density, and temperature measured earlier [13]. Gradients of the discharge plasma characteristics are calculated from the measurements of the helicon discharge plasma [12]. While there is a difference in the plasma characteristics between the helicon with and without the grids, it is assumed that the shape of the plasma contour for each characteristic is constant. This assumption, while not ideal, is sufficient for a first-order approximation of the power expended in the discharge and for the estimation of wall losses. Additionally, an ion temperature of 0.2 eV is assumed.

Since the model uses measurements of both the EHT and the GHIT, there are only two cases where the operating conditions overlap. The results of the model for these two cases are shown in table 1. The discharge efficiency is modified to use the total ion flux to the grids as the beam current in equation (4), rather than the extracted beam current. Doing so

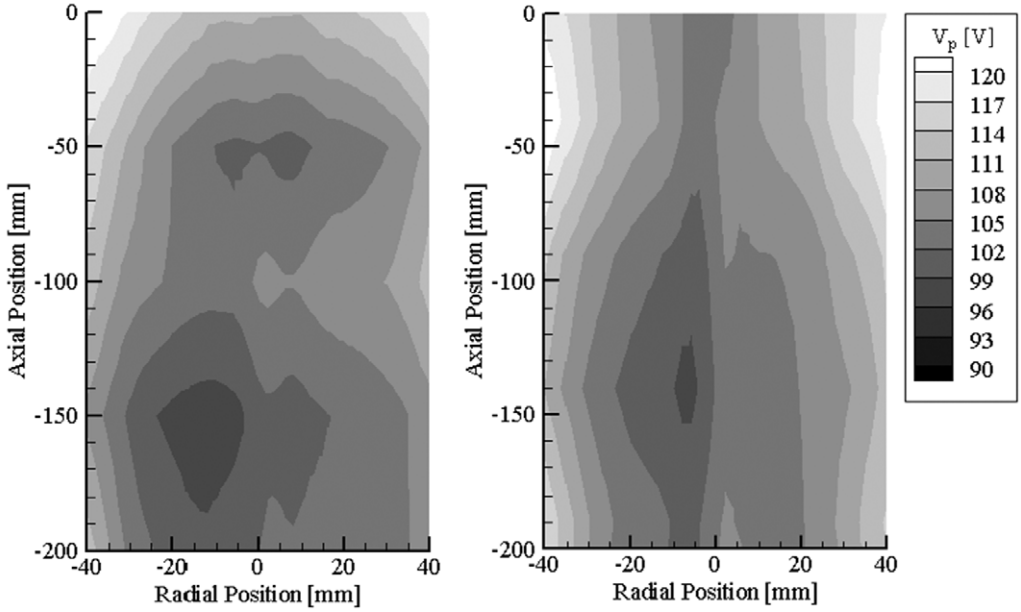

Figure 3. Plasma potential contour of the discharge chamber at 150 G (left) and 350 G (right); 600 W RF power, 1.5 mg s^{-1} Ar, 1.6×10^{-5} Torr-Ar. The axial position of 0 refers to the exit plane of the helicon.

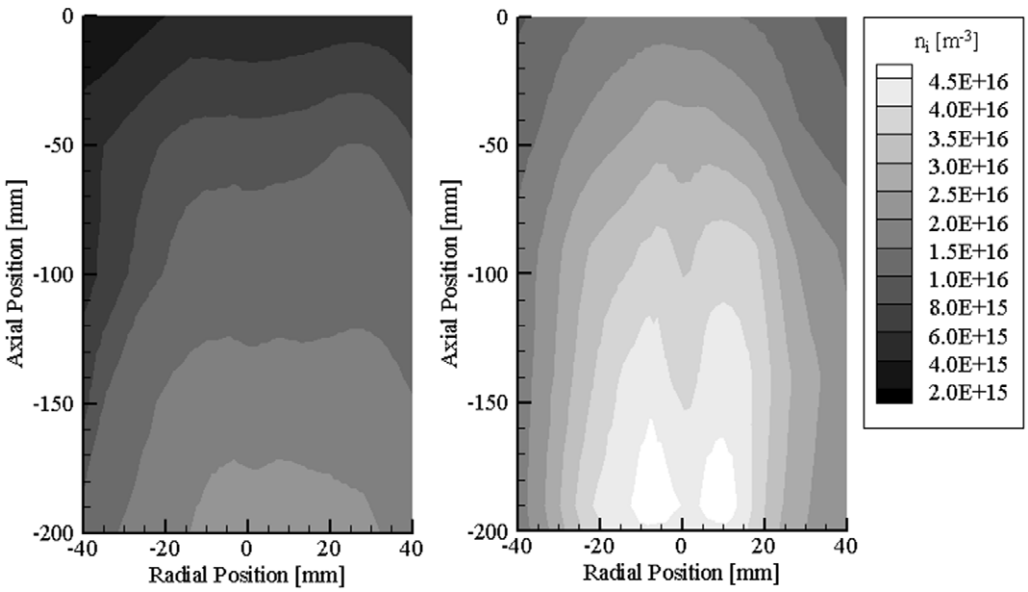

Figure 4. Ion number density contour of the discharge chamber at 150 G (left) and 350 G (right); 600 W RF power, 1.5 mg s^{-1} Ar, 1.6×10^{-5} Torr-Ar. The axial position of 0 refers to the exit plane of the helicon.

avoids combining the discharge loss with the efficacy of the ion optics of the grid assembly:

$$\eta_d = \frac{P_{abs}}{I_b + I_s + I_A}. \tag{29}$$

Therefore, the discharge efficiency represents the energy cost to create and transport an ion to the grid sheath. The discharge efficiency is higher than what is common, as a standard dc discharge chamber using argon has a discharge efficiency of approximately 150 eV.

One consideration is there is no magnetic shielding of the anode from ions for the data collected. Standard ion engine discharges provide a magnetic shield of the anode to reduce ion collection and reduce power losses. Unimpeded ion collection by the anode contributes to discharge loss by expending the power spent to create the lost ions, as well as the energy used to accelerate the ions into the anode.

The ion loss rate to the walls is found to be considerably larger than the beam current, which demonstrates that wall losses are a significant fraction of the ions created, approximately 27%. This is a consequence of the discharge chamber geometry that had a large surface-area-to-volume ratio. Ion losses can be reduced by increasing the discharge chamber diameter and decreasing the length, as this decreases the area the plasma can contact. However, further analyses will assume constant discharge chamber geometry allowing

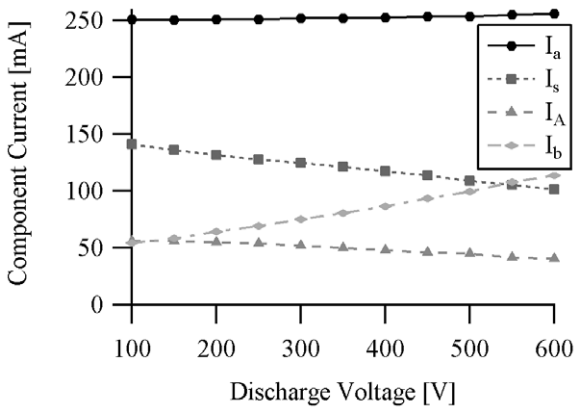

Figure 5. Component currents as a function of discharge voltage; 600 W, 100 G, 1.5 mg s^{-1} Ar, 1.6 × 10^{-5} Torr-Ar.

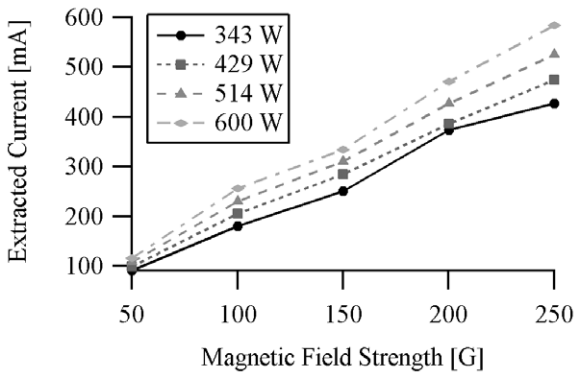

Figure 6. Extracted ion current as a function of rf power and magnetic field; 1.5 mg s^{-1} Ar, 1.6 × 10^{-5} Torr-Ar.

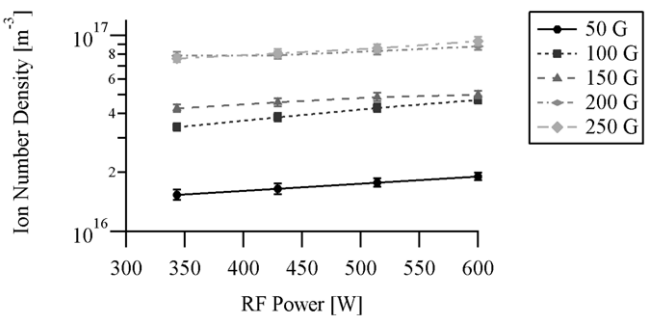

Figure 7. GHIT average ion number density as a function of rf power and magnetic field strength; 1.5 mg s^{-1} Ar, 1.6 × 10^{-5} Torr-Ar.

the use of the previously measured plasma characteristics in subsequent analyses. Instead, discussion will proceed to two parameters of the discharge plasma that have a strong impact on the ion production cost: the magnetic field strength and the electron temperature.

5.1. Magnetic field effects

The first effect of the magnetic field is to increase the ion number density of the discharge plasma. This leads to increased ion extraction and the resulting thruster currents, as well as increased power absorption by the discharge plasma.

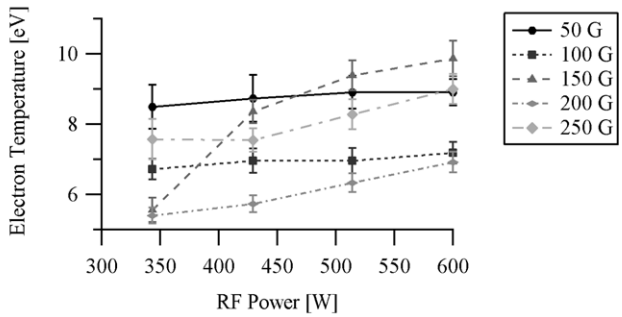

Figure 8. GHIT average electron temperature as a function of rf power and magnetic field strength; 1.5 mg s^{-1} Ar, 1.6 × 10^{-5} Torr-Ar.

Table 1. Estimated discharge performance parameters at 150 G, 600 V discharge, 1.5 mg s^{-1} Ar.

rf power (W)	Extracted current) (mA)	Wall current (mA)	Absorbed power (W)	Discharge loss (eV)
343	80.8	201	46.3	185
600	88.8	225	67.3	201

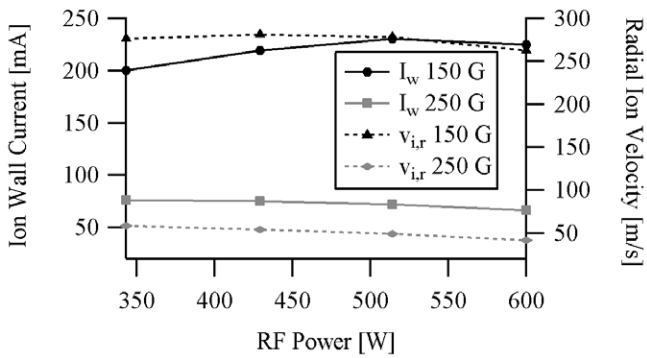

Figure 9. Estimated wall ion current and radial ion velocity as a function of rf power and magnetic field.

While this has some impact on the ion production cost, ignoring any changes to the spatial distribution of the density and resulting changes to the perveance and ion optics, the magnetic field has a greater effect on ion loss to the walls. The radial ion velocity can be reduced by increasing the magnetic field, which reduces the radial ion mobility to the wall by equation (14). A reduction in the radial ion velocity leads to decreased ion losses to the walls, which decreases the ion production cost. Figure 9 shows that increasing the magnetic field from 150 to 250 G significantly decreases the radial ion velocity and the ion-wall current. These calculations involve interpolating some of the data from the EHT measurements, as such data at 250 G or at rf power other than 343 or 600 W are not available.

Since each ion lost to the wall is an expenditure of energy that does not produce an ion for extraction and acceleration, decreasing the ion-wall loss also decreases the ion production cost. At 200 and 250 G the ion production cost is much closer to what is generally seen in dc discharges, as seen in figure 10. Further increases in the magnetic field would decrease the discharge efficiency below 150 eV, but the ion loss rate to the walls becomes too small to have a discernible effect.

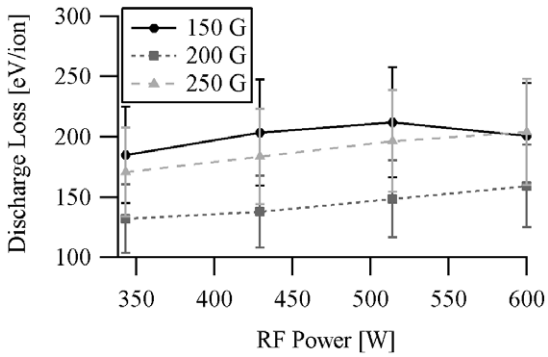

Figure 10. Discharge loss (ion cost) as a function of rf power and magnetic field for 1.5 mg s^{-1} argon.

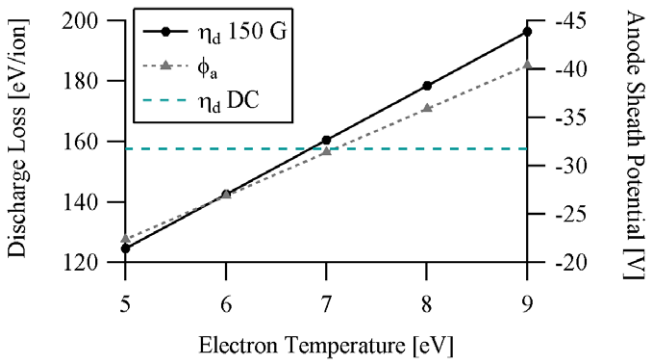

Figure 11. Predicted discharge loss (ion cost) and anode sheath potential as a function of electron temperature. The average discharge efficiency of a dc discharge chamber is shown for comparison.

That is not to say this is a clear case of diminishing returns, as thus far increasing the magnetic field demonstrates only positive enhancements to performance: increased ion density, decreased beam divergence and decreased ion production cost. However, if further decreases in ion production cost are desired, there is another source of energy loss that must be examined, one which also explains why the 200 G cases have a lower ion production cost than the 250 G cases—the discharge chamber sheaths.

5.2. Electron temperature effects

The two largest expenditures of power in the discharge are ionization of neutrals, and acceleration of ions and electrons through the boundary plasma sheaths. The first consists of the cost to create the ions that are extracted by the grids, plus an additional amount of power spent creating ions that are lost to wall neutralizations. The previous section has demonstrated that while considerable decreases in the ion production cost can be attained by decreasing wall losses, it is insufficient to decrease the ion production cost below that of standard dc discharges. The second major power expenditure occurs when ions and electrons pass through the sheaths at the boundaries of the discharge chamber. Across each sheath exists a potential drop that repels a sufficient number of electrons to balance the ion flux incident on the sheath. Each ion or electron that passes through the sheath has electric work done on it, which expends energy from the discharge plasma. Therefore, decreasing the sheath potentials will yield a further decrease in the ion production cost.

Equation (27) shows that the sheath potential has a linear dependence on the electron temperature. This arises from the fact that the sheath potential must repel a certain amount of electrons, and the repulsion force opposes the thermal kinetic energy of the electron. Higher temperature electrons have a higher kinetic energy than lower temperature electrons, and thus require a larger sheath potential. Therefore, decreasing the electron temperature of the discharge plasma decreases the anode sheath potential as well as the ion production cost. This is the cause for the 200 G cases having a lower ion production cost than the 250 G cases, as the 200 G cases have lower electron temperatures (5–7 eV compared with 7–9 eV) despite having a higher ion loss rate to the walls. Figure 11 shows an example of this effect where the 600 W condition at 150 is modeled assuming arbitrary electron temperatures. While the electron temperature is not a free variable that can be altered without other effects, it demonstrates the impact of the electron temperature on the discharge efficiency.

The results of the discharge model show that while most of these initial experiments show a higher ion production cost compared with dc discharges, a lower ion production cost is possible under certain operating conditions. The 200 G case demonstrates a discharge efficiency of 132–159 eV, which shows that such operating conditions are possible. These values are still higher than those observed in other works using helicon plasma sources [9, 10], but such experiments were performed at a higher magnetic field strength. The primary impact of such operating conditions is the increased confinement of the ions, which would not only reduce wall losses, but also restrict radial and azimuthal velocities, and reduce ion collisions and the associated losses. Additionally, the total beam current in the other works was determined using planar Langmuir probes, which can overestimate the ion current in the same manner as Faraday probes. The results of this study demonstrate that even without magnetization of the ions, the helicon plasma source is capable of a superior discharge efficiency compared with dc discharges. Further improvements to the discharge efficiency should involve examining how to use the helicon plasma source to tailor the electron energy distribution function to favor lower energy electrons that are still sufficient to ionize the propellant.

5.3. Rf power coupling

A greater concern with the results of the discharge model is that the predicted power absorbed by the plasma is only approximately 15% of the rf power transmitted to the antenna. While this model is only a first-order approximation, it demonstrates that a significant amount of power does not couple to the plasma. Another way to quantify the problem is comparing the total ion current to the propellant mass flow rate. For the 600 W case, the total ion production is estimated to be 440 mA, which is equal to 2.8×10^{18} ions s^{-1}. The mass flow rate of 1.5 mg s^{-1} yields a neutral rate of 2.3×10^{19},

which yields an ionization rate of about 12%. The amount of power needed to ionize all the propellants at the same discharge efficiency is approximately 490 W, which again demonstrates that sufficient power is available, yet is not absorbed by the plasma.

If only a fraction of the rf power is absorbed by the plasma, it is likely that the rf power is coupling to something else in addition to the plasma. Several possibilities include capacitive coupling with the thrust stand through the solenoid mounts, inductively creating eddy currents within the solenoid mounts, or coupling to the chamber at the feedthrough. The skin depth of the plasma is

$$\delta = \frac{c}{\sqrt{\omega_{\mathrm{p}}^2 - \omega^2}} \tag{30}$$

where ω_{p} is the plasma frequency given by

$$\omega_{\mathrm{p}} = \left(\frac{n_0 e^2}{\varepsilon_0 m_{\mathrm{e}}}\right)^{1/2}. \tag{31}$$

In the 600 W, 150 G case this is approximately 5 cm, so it is not the case that the plasma is insufficiently opaque to the rf wave. One method to investigate this further is to attempt to measure the directionality of the double saddle antenna. The solenoid mounts are a likely object for the antenna to couple to, as they are very close to the antenna and the aluminum cylinder that the wire is wrapped around provides a continuous loop radially around the antenna. This loop provides a pathway for the antenna to induce a circular eddy current that can resistively dissipate the rf energy. The solenoid mount is also separated from the thrust stand mount only by four 0.6 cm thick PEEK spacers. This gap creates a small capacitance, which allows the rf in the solenoid mount to capacitively couple to the thrust stand mount, and from there to ground.

One method to test this is to replace the solenoid mounts with those fabricated from insulating materials. This should both eliminate the circular path with which to induce an eddy current, and remove the capacitive path to ground. Another method to reduce rf losses is to use an in-vacuum matching network rf system configuration. This would reduce any potential coupling between the rf system and the feedthrough that might arise due to the feedthrough being a part of the matching circuit. If the matching network is relocated inside the vacuum chamber, this is less likely to occur. This would also reduce the length of transmission line that is a component of the matching circuit, which might eliminate rf coupling between the transmission line and vacuum chamber surfaces.

Another consideration is that it is unknown how much power is spent in rf excitation of neutrals and ions. The discharge efficiency model includes a term for collisional excitation, but this term is too small (on average 72 mW) to justify the visual intensity of the light emitted by the plasma. Therefore, it is highly likely that additional power is expended in rf excitation of photon emission from the argon species in the discharge chamber.

6. Conclusion

The ion production cost of a helicon plasma source has been estimated using a gridded ion extractor to definitively measure the extracted ion current. The ion production cost estimation is performed using a discharge model that utilizes measurements of the plasma potential, ion number density and electron temperature of a grid-less helicon plasma source of the same geometry, in addition to the gridded measurements. Operating conditions are 343–600 W rf power at 13.56 MHz, 50–250 G and 1.5 mg s^{-1} of argon at a pressure of 1.6×10^{-5} Torr-Ar. The helicon plasma source demonstrates an ion production cost in the range 132–212 eV/ion, which at the lower bound confirms that it is capable of meeting and exceeding the discharge efficiency of dc discharges. The primary parameters that determine the discharge efficiency are the magnetic field and the discharge plasma electron temperature. This dependence on the electron temperature yields an additional strength of the helicon plasma source, as it is capable of adapting the electron energy distribution to alter the electron temperature. This feature should be the focus of further work, as reduction in the electron temperature will further reduce the ion production cost. Further gains can be attained by adapting the helicon plasma source into a geometry more suited to use with an ion engine, such as decreasing the discharge chamber length and increasing the diameter. As a result, it can be concluded that helicon plasma sources can be used to replace dc plasma discharges given sufficient optimization.

Acknowledgments

The authors would like to thank American Pacific In-Space Propulsion for their support, the Georgia Tech Aerospace Engineering Machine Shop for fabrication and hardware support, as well as the students of the High-Power Electric Propulsion Laboratory for additional assistance.

References

[1] Chen F F 1991 Plasma ionization by helicon waves *Plasma Phys. Control. Fusion* **33** 339–64
[2] Chen F F 1995 Helicon plasma sources *High Density Plasma Sources* ed O A Popov (Park Ridge, NJ: Noyes Publications)
[3] Chen F F 1992 Experiments on helicon plasma sources *J. Vac. Sci. Technol.* **10** 1389–401
[4] Boswell R W 1984 Very efficient plasma generation by whistler waves near the lower hybrid frequency *Plasma Phys. Control. Fusion* **26** 1147–62
[5] Degeling A W, Jung D O, Boswell R W and Ellingboe A R 1996 Plasma production from helicon waves *Phys. Plasmas* **3** 2788–96
[6] Perry A J, Vender D and Boswell R W 1991 The application of the helicon source to plasma processing *J. Vac. Sci. Technol.* **9** 310–7
[7] Degeling A W, Sheridan T E and Boswell R W 1999 Intense on-axis plasma production and associated relaxation oscillations in a large volume helicon source *Phys. Plasmas* **6** 3664–73
[8] Goebel D M and Katz I 2008 *Fundamentals of Electric Propulsion: Ion and Hall Thrusters* (*Jet Propulsion Laboratory Space Science and Technology Series*) ed J H Yuen (Pasadena, CA: Jet Propulsion Laboratory)
[9] Cassady L D, Chancery W J, Longmier B W, Olsen C, McCaskill G, Carter M, Glover T W, Squire J P, Chang-Díaz F R and Bering E A III 2009 VASIMR technological advances and first stage performance results *45th AIAA Joint Propulsion Conf. (Denver, CO, 2009)* AIAA 2009–5362

[10] Reilly M P 2009 Three dimensional imaging of helicon wave fields via magnetic induction probes *Nuclear Engineering PhD Dissertation* University of Illinois, Urbana-Champaign, IL

[11] Shabshelowitz A 2013 Study of rf plasma technology applied to air-breathing electric propulsion *Aerospace Engineering PhD Dissertation* University of Michigan, Ann Arbor, MI

[12] Williams L T and Walker 2013 Plume structure and ion acceleration of a helicon plasma source *Plasma Sources Sci. Technol.* submitted

[13] Williams L T and Walker 2013 Initial performance evaluation of a gridded helicon ion thruster *J. Propulsion Power* submitted

[14] Williams L T 2013 Ion acceleration mechanisms of helicon thrusters *Aerospace Engineering PhD Dissertation* Georgia Institute of Technology, Atlanta, GA

[15] Williams L T and Walker 2013 Thrust measurements of an rf plasma source *J. Propulsion Power* **29** 520–7

[16] Reid B M 2009 The influence of neutral flow rate in the operation of Hall thrusters *Aerospace Engineering PhD Dissertation* University of Michigan, Ann Arbor, MI

[17] Raju G G 2004 Electron–atom collision cross sections in argon: an analysis and comments *IEEE Trans. Dielectr. Electr. Insul.* **11** 649–73

[18] Giannelli S, Kieckhafer A W and Walker M L R 2013 Neutral gas expansion in a cylindrical helicon discharge chamber *J. Propulsion Power* **29** 540–6

[19] Katz I, Gardner B M, Mandell M J, Jongeward G A, Patterson M and Myers R M 1997 Model of plasma contactor performance *J. Spacecr. Rockets* **34** 824–8